Volume 18
Number 10
12 March 2026
Pages 5055-5606

Nanoscale

rsc.li/nanoscale

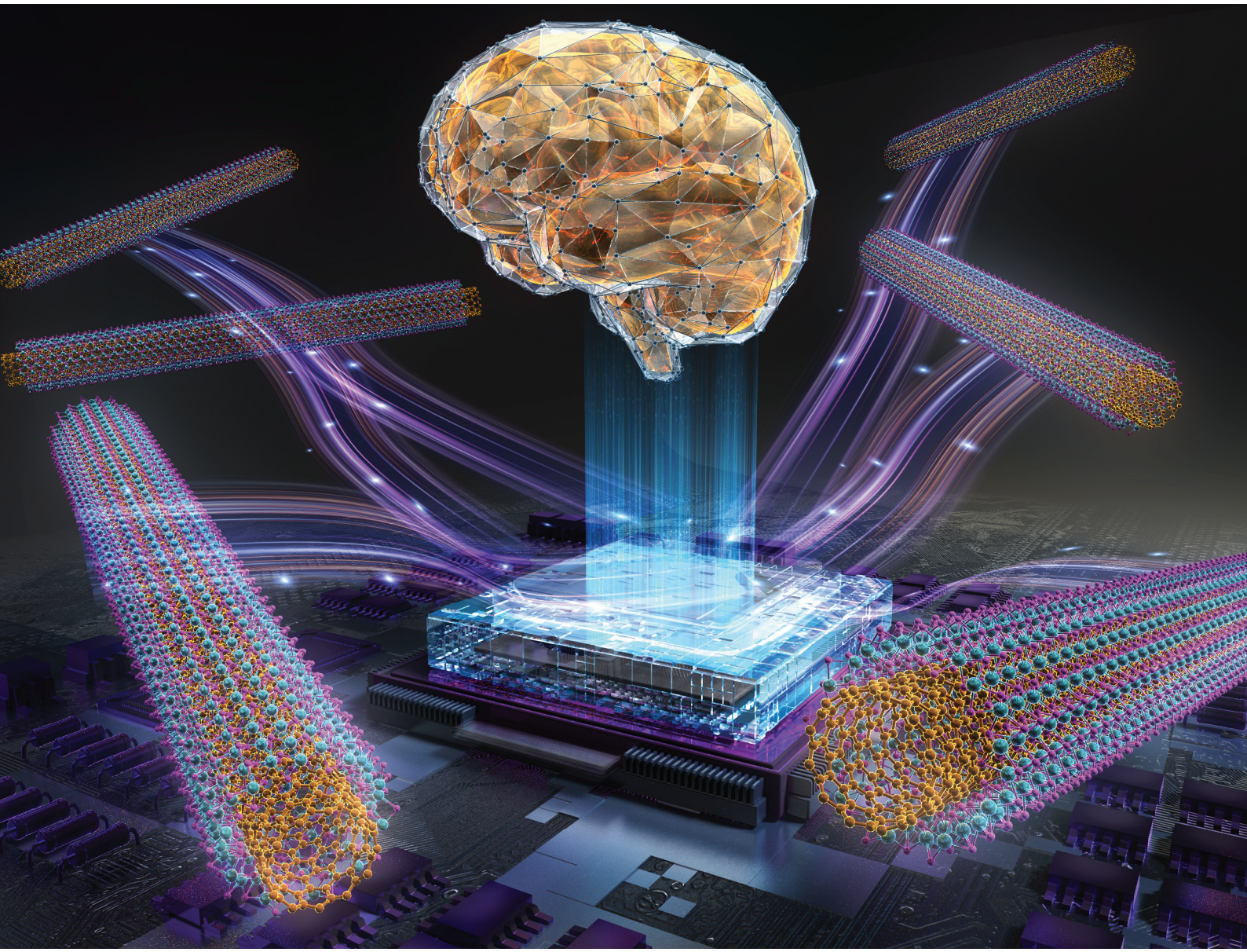

ISSN 2040-3372

ROYAL SOCIETY OF CHEMISTRY

PAPER

Hirofumi Tanaka *et al.*

$MoSe_2$/SWNT core–shell hybrids with space-charge-limited conduction and nonlinear dynamics for in-materio physical reservoir computing

NCNST

Nanoscale

PAPER

View Article Online
View Journal | View Issue

Cite this: *Nanoscale*, 2026, **18**, 5190

$MoSe_2$/SWNT core–shell hybrids with space-charge-limited conduction and nonlinear dynamics for in-materio physical reservoir computing

Alif Syafiq Kamarol Zaman, [a] Saman Azhari, [b,c] Muzhen Xu, [c] Yuki Usami [a,c] and Hirofumi Tanaka *[a,c]

This study presents the synthesis, characterization, and application of molybdenum diselenide/single-walled carbon nanotube ($MoSe_2$/SWNT) core–shell structures as a new platform for in-materio physical reservoir computing. The hybrid material was fabricated *via* a modified hydrothermal process, yielding a conductive SWNT network uniformly coated with semiconducting $MoSe_2$. Structural and electrical characterization studies (XPS, XRD, SEM, TEM, *I*–*V*, and EIS) confirm a crystalline fibrous core–shell morphology that exhibits a voltage-driven transition from a capacitive high-resistance state to a space-charge-limited conduction (SCLC) regime. Physical reservoir computing based on $MoSe_2$/SWNTs thus leverages SCLC dynamics, where trap-controlled transport generates higher harmonics and short-term memory, providing the essential nonlinearity and fading memory required for temporal processing. Consequently, the $MoSe_2$/SWNT device achieves strong performance in benchmark tasks, including waveform reconstruction (NMSE < 0.1 across multiple periodic functions), NARMA2 time-series prediction (90% accuracy), and memory capacity evaluation. These results establish a direct link between device physics and computational capability, highlighting $MoSe_2$/SWNT hybrids as a scalable candidate for next-generation neuromorphic hardware.

Received 20th September 2025,
Accepted 28th December 2025

DOI: 10.1039/d5nr03974f

rsc.li/nanoscale

1. Introduction

The rapid advancement of materials science has catalysed the development of novel nanostructures with unique electrical and electrochemical properties, making them promising candidates for physical reservoir computing (PRC) and hardware implementations of neuromorphic computing systems.[1–4] PRC leverages the inherent dynamic behaviours of physical systems to perform complex information processing tasks,[5,6] offering a simplified training process and significantly reduced power consumption compared to conventional recurrent neural networks. This approach makes PRC an attractive solution for overcoming the limitations of traditional von Neumann architectures,[2,5–7] particularly in applications such as time-series prediction, classification, and pattern recognition. The core principle of PRC involves transforming input signals into a high-dimensional state space using a dynamic reservoir, followed by a simple linear classification or regression.[8,9] The reservoir, composed of a network of nonlinear elements, is essential for providing the nonlinearity and memory required to capture temporal dependencies. PRC has demonstrated success across various domains, including robotics, autonomous systems, and emulation of biological neural networks.[8–20]

Among the various nanostructures investigated for in-materio PRC, memristive nanowire networks have attracted significant attention due to their self-organizing, designless nature that mimics the topology and emergent behaviours of biological neuronal circuits.[21–25] Noteworthy examples include Ag nanowire random networks[19,21,23,26–31] and Ag–Ag_2S core–shell nanoparticle networks,[32–39] which typically rely on metallic or filamentary conduction to generate nonlinear dynamics. Alongside these filamentary systems, reservoirs such as sulfonated polyaniline networks[20] and single-walled carbon nanotubes and polyoxometalate (SWNT/POM),[40] as well as iodobismuthate complexes,[41] which exhibit redox-based conduction, have been explored and have shown high proficiency in waveform reconstruction and temporal pattern recognition in reser-

[a]*Graduate School of Life Science and Systems Engineering, Kyushu Institute of Technology, 2-4 Hibikino, Wakamatsu, Kitakyushu, 808-0196 Japan. E-mail: tanaka@brain.kyutech.ac.jp*
[b]*Graduate School of Information, Production and Systems (IPS), Waseda University, 2-7 Hibikino, Wakamatsu, Kitakyushu, 808-0135 Japan*
[c]*Research Center for Neuromorphic AI Hardware, Kyushu Institute of Technology, 2-4 Hibikino, Wakamatsu, Kitakyushu, 808-0196 Japan*

voir tasks. In addition, semiconducting polymers like P3HT[42] have demonstrated nonlinear responses arising from molecular orientation effects, further broadening the range of explored materials. Despite progress in the development of metal/insulator core–shell nanostructures and semiconducting polymer nanowires, the potential of metal/semiconductor core–shell nanostructures for PRC remains underexplored. Such hybrid systems are particularly attractive because they can merge efficient charge transport from a conductive network with the tuneable nonlinearity of a semiconductor shell, enabling both stability and richer temporal dynamics. In particular, molybdenum diselenide/single-walled carbon nanotube ($MoSe_2$/SWNT) core–shell structures combine the exceptional electrical conductivity of SWNTs[43] with the semiconducting nature of $MoSe_2$,[44–47] offering enhanced electrochemical activity, high surface area, and unique nonlinear dynamics.

$MoSe_2$/SWNT hybrids have already been applied in diverse fields, such as solar cells,[48–50] photonics,[14] optoelectronics,[51–53] sensors,[54] hydrogen evolution,[55–60] supercapacitors,[61,62] and batteries.[63–65] However, their potential for PRC applications has remained largely untapped. The intrinsic properties of these hybrids, specifically their rich nonlinear response and dynamic charge transport, align closely with the fundamental requirements of PRC. Previous in-materio PRC devices show that the conduction mechanism strongly influences the task performance. Ag_2S islands,[36,38] Ag–Ag_2S nanoparticle systems,[32–35] and Ag nanowire systems[21,28,29] rely on filamentary switching, which can produce nonlinear dynamics but often leads to variability in waveform and NARMA tasks. Redox-based systems, such as sulfonated polyaniline networks,[20] iodobismuthate complexes,[41] nickel complexes,[66] and SWNT/POM[40,67] hybrids have achieved good task performance, yet their reliance on faradaic processes can introduce variability and limit harmonic preservation. Semiconducting polymers such as P3HT,[42] on the other hand, exhibit orientation-dependent conduction that supports certain temporal tasks but provides limited harmonic richness. In contrast, the $MoSe_2$/SWNT hybrid operates in an SCLC regime, where trap-controlled conduction generates higher harmonics and short-term memory, providing a more favourable basis for achieving high accuracy in diverse AI benchmarks. Recent studies on electrochemical reactions and nonlinear dynamics in similar composites further underscore their suitability for such applications.[40,55]

Conventional $MoSe_2$-based devices typically employ vertical or sandwich-type architectures with filamentary conduction mechanisms,[47,68,69] which can compromise device reproducibility and scalability. In contrast, our approach utilizes $MoSe_2$/SWNT hybrids with non-reactive aluminium electrodes in a horizontal architecture. This design intentionally suppresses the extrinsic filamentary effects (*i.e.*, electrochemical metallization) often associated with active electrodes like Ag, shifting the conduction mechanism toward intrinsic, bulk-limited space-charge-limited conduction (SCLC). This design emphasizes intrinsic resistive switching over extrinsic filamentary effects, offering improved suitability consistent switching dynamics, utilizing the random network's heterogeneity for high-dimensional projection while maintaining stability through bulk-dominated conduction. Additionally, the SWNT network plays a critical role in enhancing electrical conductivity and fostering the essential non-linear dynamics required for PRC.[70] By systematically investigating the synthesis, characterization, and PRC performance of $MoSe_2$/SWNT hybrids, this study bridges a critical gap in current research and highlights a promising pathway toward stable, scalable, and energy-efficient neuromorphic computing devices. Our work introduces a novel materials platform that synergistically combines designless self-organization with intrinsic nonlinear dynamics, paving the way for the development of next-generation AI hardware capable of supporting edge computing, robotics, and energy-efficient, thereby addressing the urgent demand for greener and smarter computational technologies.

2. Experimental method

2.1. Synthesis of the $MoSe_2$/SWNT core–shell structure

$MoSe_2$/SWNT composites were synthesized following an approach adapted from several methods, with modifications of the precursor amounts and SWNT content.[47,71] All chemicals were purchased from Sigma-Aldrich, except for hydrazine hydrate ($N_2H_4{\cdot}H_2O$, 97%), which was obtained from Wako. To start the synthesis, 0.5 mmol of sodium molybdate dihydrate ($Na_2MoO_4{\cdot}2H_2O$) and 1 mmol of selenium powder were used as precursors. To prepare the precursor solution, sodium molybdate was dissolved in a mixture of 20 mL of deionized (DI) water and 10 mL of ethanol together with varying amounts of SWNTs (0 mg, 1 mg, 5 mg, and 10 mg). Separately, selenium powder was dissolved in 10 mL of hydrazine hydrate under magnetic stirring at room temperature, resulting in a dark red solution that confirmed the formation of the selenium precursor. The two solutions were combined and transferred to a Teflon-lined stainless-steel autoclave, which was then sealed and heated at 180 °C for 12 hours to facilitate the hydrothermal reaction and form the $MoSe_2$/SWNT composite. After the reaction, the product was thoroughly washed several times with ethanol and DI water to remove residual reactants and by-products. The final $MoSe_2$/SWNT powder was filtered and dried in an oven at 70 °C. This modified synthesis yields composites with systematically varied SWNT content, enabling a detailed investigation of the effects of precursor concentration and SWNT loading on material properties.

2.2. Structural characterization

X-ray diffraction (XRD) spectroscopy was performed using a Rigaku Smart Lab with a Cu Kα source. X-ray photoelectron spectroscopy (XPS) (Kratos Axis) with a monochromatic Al Kα X-ray source was utilized. Scanning electron microscopy (SEM) was performed using a Thermo Scientific Quattro SEM and transmission electron microscopy (TEM) was performed using a JEOL JEM-2100 Plus.

2.3. Electrical characterization

I–V measurements were performed using a semiconductor parameter analyser (Keysight B1500A). *V–t* measurements were performed using a data acquisition (DAQ) system (National Instruments PXIe-6363 and SCB-68A). A custom LabVIEW program was used to apply input signals and record the output responses. Electrochemical impedance spectroscopy (EIS) measurements were performed using a Zurich MFIA impedance analyser. In these plots, the imaginary component of impedance (Z'') is plotted against the real component (Z'), obtained from absolute impedance and phase angle measurements across a frequency range of 1 Hz–1 MHz The DC offset voltage was varied from 0 V to 5 V, while the AC perturbation signal had an amplitude of 300 mV. The Nyquist plots were fitted using free EIS analyser software, Yappari.[72] In this study, a simplified Randle's circuit was employed, consisting of a single resistor R_p in parallel with a constant-phase element (CPE).[70,73] The total impedance is described by:

$$Z(\omega) = [(1/R_p) + Q(j\omega)^n]^{-1} \quad (1)$$

where Q (Ω^{-1} s^n) is the CPE coefficient and n is the CPE exponent. The characteristic time constant for this parallel branch is:

$$\tau = (R_p Q)^{\frac{1}{n}} \quad (2)$$

2.4. PRC Tasks

We employed a 16-electrode $MoSe_2$/SWNT device as the physical reservoir following previous methods where one electrode was used for the input and 15 electrodes for outputs.[8,15,20,42] Devices were fabricated on thermally oxidized SiO_2/Si substrates. A 16-electrode aluminium (Al) array (50 nm thick, 100 μm gap) was patterned using standard photolithography with a chromium photomask, followed by sputtering (base pressure 10^{-5} Torr) and a bi-layer lift-off process. The synthesized $MoSe_2$/SWNT composite was dispersed in ethanol (40 mg mL^{-1}), and 3 μL of the solution was drop-cast onto the central electrode gap at 70 °C. The chip was then packaged on PCB and wire-bonded with silver paste for measurements. Full fabrication details are provided in the SI.

The schematic for the setup is shown in Fig. 1a and b, where the device was driven by an external input signal $u(t)$ and the resulting voltages at each electrode, $O_i(t)$ for $i \in \{1,\ldots, N\}$, were recorded at discrete time steps t. These electrode outputs collectively form the reservoir state vector:

$$x(t) = \begin{bmatrix} O_1(t) \\ O_2(t) \\ \vdots \\ O_N(t) \end{bmatrix} \quad (3)$$

where N is the total number of electrodes (*e.g.*, N = 15). In a typical software-based reservoir, one would define an explicit update equation, but in our approach, the device's intrinsic memristive and electrochemical properties govern the transformation from $x(t)$ and $u(t)$ to $x(t+1)$. Symbolically, we can write:

$$x(t+1) = f_{\text{device}}(x(t), u(t)) \quad (4)$$

where f_{device} represents the physical dynamics of the $MoSe_2$/SWNT material. Because these dynamics are embodied in the device, we do not need an explicit functional form; we simply measure $x(t)$ at each time step.

2.4.1. Readout training. To map the measured reservoir states $x(t)$ to a target output $y(t)$, a linear readout *via* ridge regression is trained. The predicted output $\hat{y}(t)$ is a linear combination of these states with readout weights w_i, given by:

$$\hat{y}(t) = \sum_{i=1}^{15} w_i O_i(t) \quad (5)$$

For compactness, we can write this in vector form as:

$$\hat{y}(t) = W_{\text{out}} x(t)$$

where $W_{\text{out}} = (w_1, w_2, \ldots, w_{15})^T$ is the readout weight vector and $x(t) = (O_1(t), O_2(t), \ldots, O_{15}(t))^T$ is the reservoir state vector. During ridge regression, the readout weights are trained by minimizing the following cost function:

$$J(W_{\text{out}}) = \sum_{t=1}^{T} (y(t) - \hat{y}(t))^2 + \lambda |W_{\text{out}}|^2 \quad (6)$$

where λ is the regularization parameter. The value is automatically optimized using grid search and cross-validation for all PRC tasks, which was then applied in the ridge regression readout to mitigate overfitting and ensure stable training performance. This value was determined empirically and provided a suitable balance between model complexity and numerical robustness. The closed-form solution for ridge regression is:

$$W_{\text{out}} = (X^T X + \lambda I)^{-1} X^T Y \quad (7)$$

where $X \in^{T \times 15}$ the reservoir state matrix and $Y \in^{T \times 1}$ is the target signal vector.

2.4.2. Performance metric. To assess how accurately the reservoir system reproduces the target signal, we used the normalized mean square error (NMSE). This metric is computed separately for both the training and testing phases:

$$\text{NMSE} = \frac{1}{T} \frac{\sum_{t=1}^{T} (y(t) - \hat{y}(t))^2}{{\sigma_y}^2} \quad (8)$$

In this expression, T denotes the number of time steps in the respective evaluation interval (either training or testing). The terms $y(t)$ and $\hat{y}(t)$ represent the target signal and the predicted output at time t, respectively. The denominator ${\sigma_y}^2$ is the variance of the target signal computed over the same interval. By normalizing the mean square error by the signal variance, the NMSE provides a scale-independent measure of predictive performance, allowing comparisons across different signal types or amplitudes.

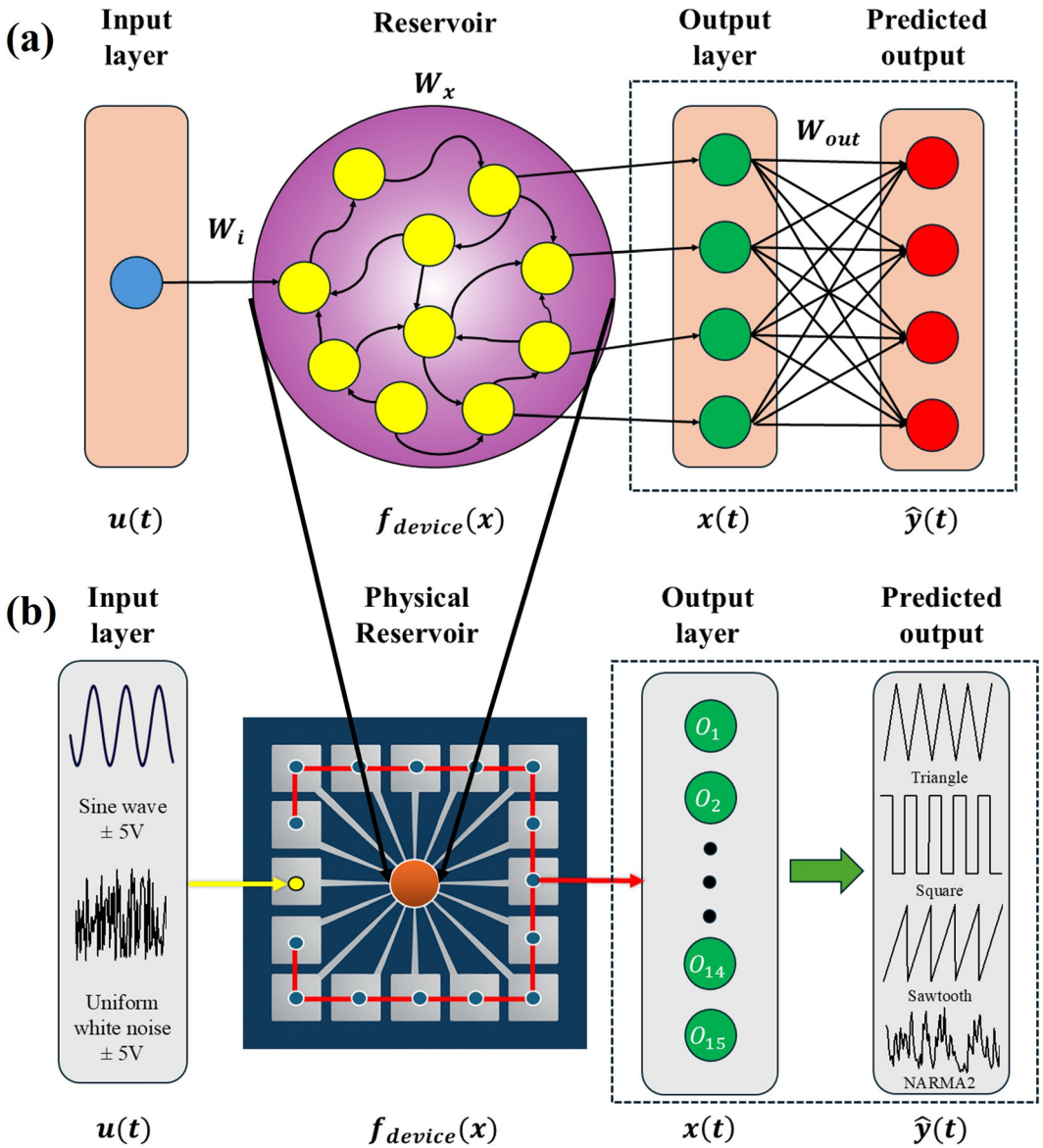

Fig. 1 (a) General framework: the input signal $u(t)$ is projected into a high-dimensional nonlinear dynamical system (reservoir), where the internal states $x(t)$ are generated through recurrent connections. The output layer is trained by adjusting only the readout weights W_{out} to approximate the target signal $\hat{y}(t)$. (b) Experimental/implementation schematic: a sine wave or uniform white noise input of ±5 V is injected into the physical reservoir. The reservoir dynamics are sampled to produce output states ($O_1(t)$,$O_2(t)$,...,$O_{15}(t)$), which are linearly combined to reproduce different target functions such as triangle, square, and sawtooth waves, as well as the NARMA2 benchmark task.

2.4.3. Waveform reconstruction task. In the waveform reconstruction task, an 11 Hz sine wave with an amplitude of 10 V_{pp} was applied as the input to the $MoSe_2$/SWNT device, and the resulting signals at the 15 electrodes were recorded as the reservoir state. A linear readout layer was then trained to map these 15 electrode outputs to the desired target waveform. Specifically, the readout weights were obtained *via* ridge regression to minimize the difference between the predicted and actual waveforms, and the performance was quantified by the NMSE. This procedure ensured that the reservoir's intrinsic nonlinear dynamics were effectively harnessed to reconstruct the input waveforms with high accuracy.

2.4.4. NARMA2 task. For this task, the input to the device was uniform white noise $u(k)$ within the range 0–5 V. This input was normalized and mapped to the range 0–0.5 V during the training phase to ensure numerical stability.[74,75] The raw uniform white noise input sequences and the corresponding recorded reservoir responses for this task are visualized in Fig. S5. Without normalization, the calculations could potentially diverge, causing instability and leading the system to unpredictable behaviours or infinite values. Normalizing the input helps to mitigate this risk and ensures that the device operates within a manageable dynamic range throughout the task. The NARMA2 target is generated using the following equation:[74]

$$y_t(k+1) = 0.4y_t(k) + 0.4y_t(k)y_t(k-1) + 0.6u^3(k) + 0.1 \quad (9)$$

This task followed the same experimental protocol as the waveform reconstruction task, differing only in the nature of the input signal and the target sequence being predicted.

2.4.5. Memory capacity. For the memory capacity experiment, the input was uniform white noise, like the NARMA2 task, but mapped to the range of −1 to 1 V for numerical stability and consistency with standard memory capacity experiments.[74,76] The reason for this mapping is that it is a common practice in memory capacity evaluations to ensure that the input remains within a bounded range, allowing for a better assessment of how the system handles information retention without the risk of instability. We then trained the readouts to predict delayed versions of the input $u(t-k)$ for delays k = 1,2,...,K. The memory capacity MC is computed as the sum of the squared correlation coefficients $r^2(k)$ between the predicted and actual delayed inputs given by:

$$\mathrm{MC} = \sum_{k=1}^{K} r^2(y,\hat{y}_k); \quad r^2(y,\hat{y}_k) = \frac{(\mathrm{cov}(y(t-k),\hat{y}(t)))^2}{\mathrm{var}(y(t-k)) \cdot \mathrm{var}(\hat{y}(t))} \quad (10)$$

where $r^2(y,\hat{y}_k)$ represents the squared correlation between the true past input $y(t-k)$ and the predicted output $\hat{y}(t)$. Here, cov $(y(t-k),\hat{y}(t))$ is the covariance between the two signals and var $(\cdot)$ denotes their respective variances. A higher MC value indicates that the reservoir retains past inputs over a longer timescale, reflecting its short-term memory performance.

3. Results and discussion

3.1. Material characterization

The material characterization of the $MoSe_2$/SWNT composite was carried out using multiple complementary techniques, as shown in Fig. 2. The XPS full survey spectrum (Fig. 2a) displays distinct peaks for Mo 3d, Se 3d, C 1s, and O 1s, confirming that molybdenum, selenium, and carbon are the key constituents of $MoSe_2$ and SWNTs. In the high-resolution XPS spectrum of Mo 3d (Fig. 2b), peaks at 228.4 eV, 231.6 eV, and 235.8 eV are observed, corresponding to the Mo^{4+} and Mo^{6+} oxidation states.[43,77,78] The appearance of Mo^{6+} suggests some surface oxidation during synthesis, which could potentially benefit the device's electrical properties. Similarly, the Se 3d spectrum (Fig. 2c) shows peaks at 54.34 eV and 55.59 eV, which are characteristic of Se^{2-} in $MoSe_2$.[71,79] This indicates that selenium is present in its expected oxidation state, suggesting that the material retains its stoichiometric composition, which is important for its semiconducting properties.

The X-ray diffraction (XRD) pattern of the $MoSe_2$/SWNT composite (Fig. 2d) exhibits distinct reflections at 2θ values of 12°, 25°, 33°, 41°, 46°, and 54°, corresponding to the (002), (004), (100), (006), (105), and (110) planes of hexagonal 2H-$MoSe_2$, respectively.[60,80] These features confirm the successful formation of crystalline $MoSe_2$ within the composite, consistent with its layered structure and indicative of good crystallinity, which is an essential attribute for maintaining reliable interlayer charge transport and electrochemical activity. Although the composite contains SWNTs, characteristic graphitic peaks typically observed near 25–26° of 2θ, which are associated with the (002) reflection of sp^2 carbon frameworks, are not clearly resolved. This absence can be attributed to the inherently broad and low-intensity diffraction features of SWNTs, their possible amorphous or turbostratic arrangement, and the overlap with the $MoSe_2$ (004) reflection at 25.2°. Such peak suppression or convolution is commonly reported in $MoSe_2$ SWNT hybrid systems, especially when the carbonaceous component is present in low concentrations or is well-dispersed at the nanoscale.[43,71,81]

The SEM image (Fig. 2e) provides additional insight into the composite's morphology. The image reveals that the SWNTs form a highly interconnected network, which likely enhances the charge transport properties by offering multiple conductive pathways throughout the nanocomposite. $MoSe_2$ appears to coat this SWNT network uniformly, combining the high surface area of the nanotubes with the functional properties of $MoSe_2$. This uniform coating is essential for facilitating both charge injection and retention, which is critical for the enhanced switching and conduction behaviours observed in electrical measurements such as *I–V* and SCLC.

The TEM image (Fig. 2f) further elucidates the composite's microstructure. The TEM analysis reveals a fibrous core–shell structure where $MoSe_2$ forms a shell encapsulating the core of SWNT bundles rather than individual nanotubes. This core–shell assignment is further supported by EDS elemental mapping, where Mo and Se signals co-localize around the carbon-rich SWNT bundles (Figure S1). This morphology is characterized by distinct contrast differences that indicate a layered coating, suggesting that $MoSe_2$ forms a shell structure over SWNT bundles.[43,77] The core–shell interface appears well-defined, though not entirely uniform, and is crucial for charge transport because it influences electronic pathways. The TEM image also shows discontinuities in the $MoSe_2$ shell, which may indicate regions of incomplete coating. These structural features could lead to localized variations in electrical characteristics, potentially affecting the overall device behaviour, including resistive switching and neuromorphic performance.

3.2. Electrical characterization

The junctions formed between $MoSe_2$ and SWNTs play a critical role in the conduction of mechanisms and nonlinear behaviour of these hybrid structures. The random network of these nanojunctions creates a complex pathway for electron transport, contributing to the overall nonlinearity observed in the system. Research indicates that these nanojunctions can lead to the formation of localized states and trap sites, which significantly influence the charge transport properties.[82–84] Zhang *et al.* discussed how the interfaces in nanostructured materials like $MoSe_2$/SWNTs can result in diverse charge transport behaviours, including SCLC and trap-controlled conduction mechanisms.[85] These mechanisms are essential for the resistive switching behaviour observed in PRC applications. Furthermore, the random network configuration of $MoSe_2$/

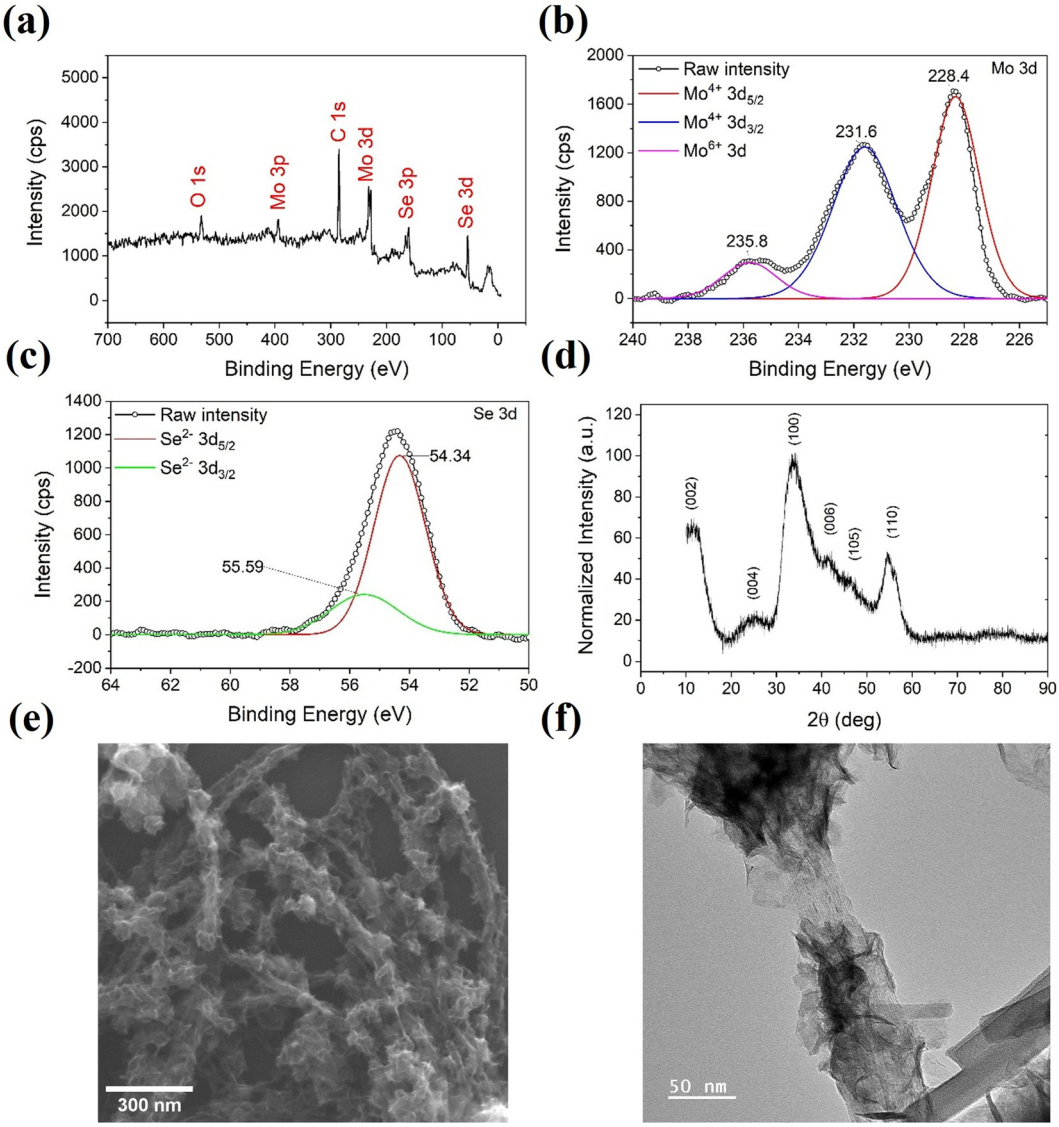

Fig. 2 (a) XPS survey spectrum of the $MoSe_2$/SWNT composite confirming the presence of Mo, Se, C, and O, (b) XPS spectrum of Mo 3d showing mixed oxidation states, (c) XPS spectrum of Se 3d indicating selenium in its reduced state, (d) XRD pattern revealing the characteristic diffraction peaks of the hexagonal $MoSe_2$ phase, (e) SEM image showing an interconnected SWNT network uniformly coated with $MoSe_2$, and (f) TEM image displaying a fibrous core–shell structure where $MoSe_2$ forms a shell around bundles of SWNTs with a defined interface and some discontinuities.

SWNT hybrids can enhance the reservoir's richness by providing multiple, diverse conduction pathways. This network complexity is beneficial for PRC, as the structural randomness creates the diverse, high-dimensional internal states required for nonlinear transformation. Furthermore, while individual nano-junctions exhibit variability, the high density of the SWNT network (5 mg loading) ensures that the macroscopic response is governed by ensemble averaging.[86,87]

The *I–V* characteristics of the $MoSe_2$/SWNT memristive devices were measured for different concentrations of SWNTs (0 mg, 1 mg, 5 mg, and 10 mg) to evaluate the impact of SWNT content on the electrical behaviour and switching dynamics. The pure $MoSe_2$ device (0 mg of SWNTs, Fig. 3a) exhibited a near-linear *I–V* curve with a slight curvature at higher voltages, suggesting limited nonlinear behaviour and a lack of pronounced resistive switching. The observed response is consistent with a predominantly semiconducting material exhibiting weak space-charge effects at higher voltages. In contrast, the device containing 1 mg of SWNTs (Fig. 3b) shows a more pronounced nonlinearity in its *I–V* characteristics, with the emergence of a hysteresis loop, indicating resistive switching behaviour. This suggests that the inclusion of SWNTs enhances charge transport by increasing conductivity and enabling charge trapping and releasing mechanisms, essential for memristive switching.

As the SWNT content increases to 5 mg (Fig. 3c), the device exhibits stronger resistive switching, exhibiting a clear counterclockwise hysteresis loop with a sharper transition between

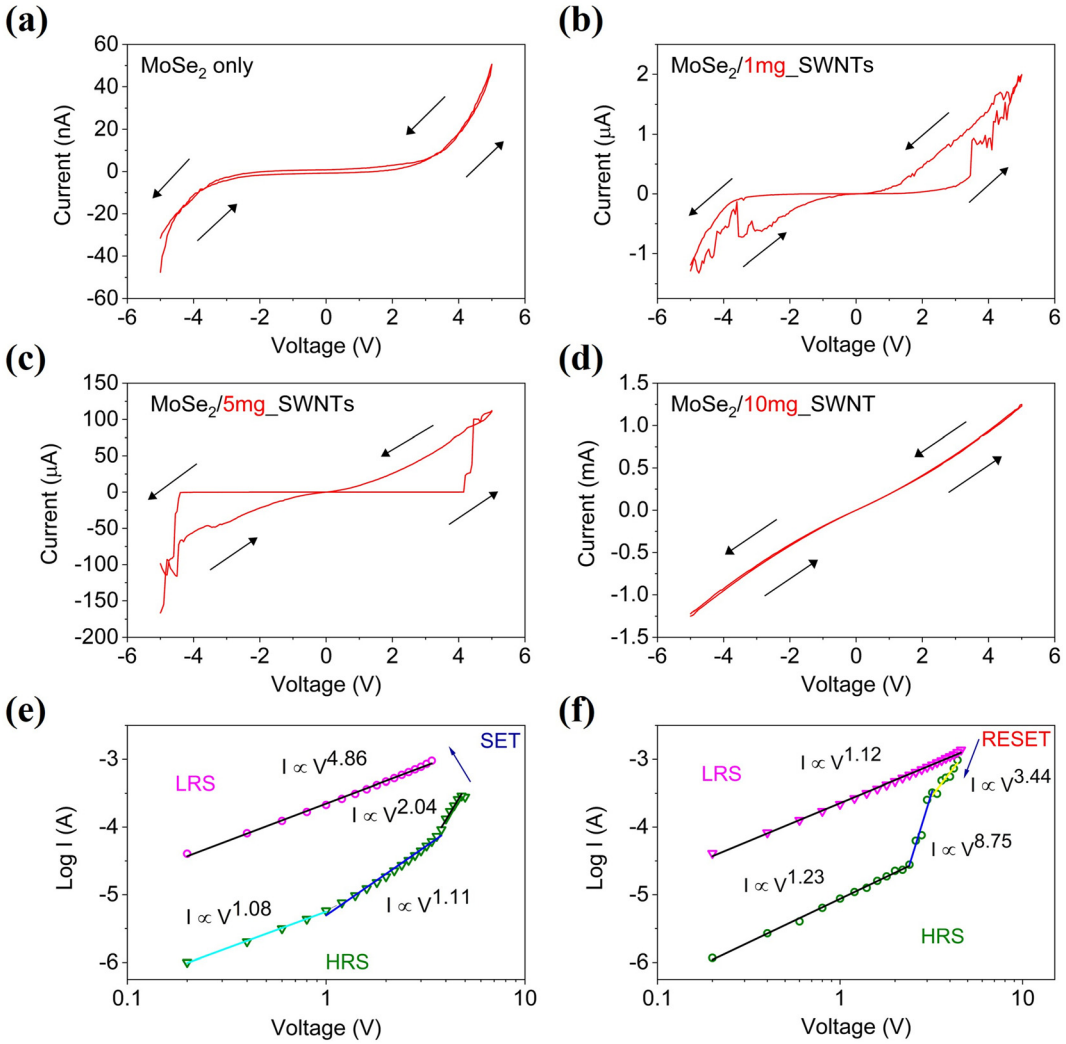

Fig. 3 *I–V* curves showing the emergence of memristive behaviour with increasing SWNT content, confirming the role of the hybrid structure in nonlinear conduction. (a) *I–V* curve for pure $MoSe_2$, (b) *I–V* curve for $MoSe_2$ with 1 mg of SWNTs showing the emergence of a counter-clockwise hysteresis loop (arrows indicate the sweep direction), (c) *I–V* curve for $MoSe_2$ with 5 mg of SWNTs exhibiting enhanced resistive switching, (d) *I–V* curve for $MoSe_2$ with 10 mg of SWNTs displaying near-linear behaviour, (e) log–log plot of the SET transition for the 5 mg device (from c), and (f) log–log plot of the RESET transition for the 5 mg device (from c), both confirming SCLC conduction mechanisms.

the high and low resistance states. The *I–V* curve shows a larger hysteresis window, which indicates enhanced charge storage capability and more significant nonlinearity in the transport characteristics. This is likely due to the increased percolation pathways provided by the SWNT network, facilitating more efficient charge injection and trapping.[88] At the highest SWNT concentration (10 mg, Fig. 3d), the *I–V* curve displays continuous, near-linear behaviour with minimal hysteresis, suggesting that the device's conductance is now dominated by the SWNT network. The lack of pronounced resistive switching at this concentration could be attributed to the formation of a highly conductive percolation network, which bypasses the trap-controlled SCLC regime observed at lower SWNT concentrations. Here, the SWNT network likely provides a low-resistance path for charge carriers, diminishing the switching characteristics observed at lower concentrations. These results highlight the critical role of SWNT content in tuning the memristive behaviour of the device. At low SWNT concentrations, the device shows strong switching characteristics, ideal for applications in neuromorphic computing where nonlinear transformations are required. However, at higher concentrations, the device becomes highly conductive, which could be better suited for applications requiring high-speed, low-resistance switching.

Building on the *I–V* analysis of the optimal 5 mg device (Fig. 3c), the log–log plot provides further confirmation of the conduction mechanism in both the high-resistance state (HRS) and the low-resistance state (LRS), as well as the SET and RESET transitions. In both plots (Fig. 3e for the SET transition and Fig. 3f for the RESET transition), distinct regions corresponding to different conduction mechanisms are evident, consistent with the SCLC model. In the HRS, the current follows a

power-law dependence on the voltage ($I \propto V^n$, where $n > 1$), indicating the presence of trap-controlled SCLC. This behaviour is more prominent in intermediate voltage ranges, where the traps within the $MoSe_2$/SWNT matrix are progressively filled by injected carriers. The transition to the LRS occurs when the traps are fully filled, and the current increases more rapidly with voltage, reflecting a transition into a trap-free SCLC regime.[47] During the RESET and SET transitions, the steep slope in the log–log plot indicates a rapid increase consistent with trap filling/TFL-related transition, which is characteristic of charge injection from the electrodes and the filling of deeper traps.[89] This further supports the observation from the *I–V* curves that the memristive switching behaviour is driven by the modulation of space-charge regions within the device. Overall, the combined analysis of the *I–V* characteristics and log–log plots confirms the dominant role of SCLC in the charge transport mechanism of the $MoSe_2$/SWNT device. This power-law behaviour, resulting from the use of non-reactive Al electrodes, is consistent with other studies on similar TMD-based memristors where SCLC is identified as the dominant intrinsic conduction mechanism.[47,89]

This bulk-dominated transport also confers significant energy advantages. Based on the static current in the LRS at a read voltage of 0.1 V and the estimated junction density, the static power consumption is approximately 0.006 nW per $MoSe_2$/SWNT junction. This is notably lower than the values reported for other random network reservoirs such as 0.07 nW per junction in Ag_2Se networks[8] and 0.02 nW per domain in $YMnO_3$.[90] These results highlight the potential of the $MoSe_2$/SWNT platform for ultra-low-power neuromorphic applications.

3.3. Electrochemical impedance spectroscopy

The electrical behaviour of the $MoSe_2$/SWNT core–shell memristive structure was investigated using EIS and current–voltage (*I–V*) measurements to elucidate its charge transport mechanisms. The EIS data reveal a voltage-dependent evolution of a single, depressed semicircle from a highly resistive state at low voltages (0–2 V) to a lower-resistance state at higher voltages (3–5 V), consistent with resistive switching behaviour, as shown in Fig. 4. The parameters extracted from fitting the spectra with an *R*||CPE equivalent circuit at each bias (resistance *R*, CPE magnitude *Q*, exponent, and the corresponding characteristic time constant τ) are summarized in Table 1.

At low voltages (0 V–1 V), the Nyquist plot rises steeply from the origin and forms only an incomplete arc, suggesting that the system is dominated by capacitive behaviour. The high resistance ($R \approx 1000$ MΩ) and large constant phase element (CPE) values indicate significant charge trapping within the $MoSe_2$ shell and at the $MoSe_2$/SWNT interface, restricting current flow. The high-resistance state (HRS) is attributed to the Schottky-like barriers at the metal–semiconductor junction and deep trap states in the $MoSe_2$ shell, which limit carrier injection. This behaviour is consistent with trap-controlled charge storage effects superimposed on bulk-limited transport rather than purely Ohmic conduction in the low-bias regime.[91] As the voltage increases to 2 V, the Nyquist plot starts to show some curvature, reflecting a reduction in resistance (R = 246 MΩ) and the onset of conduction, though the spectrum is still dominated by a single, incompletely formed semicircle and the capacitive contribution remains strong. The incomplete semicircle indicates that while some charge transport pathways are beginning to form, the device has not fully transitioned to a conductive state.

At 3 V, a clear semicircle appears in the Nyquist plot, corresponding to a significant reduction in resistance (R = 76.1 MΩ). This marks the transition to a low-resistance state (LRS), where conductive pathways, likely facilitated by the SWNT core, have been established. The appearance of this semicircle suggests that the capacitive components are becoming less dominant, and the system is now characterized by both resistive and capacitive contributions. The fitted *R*||CPE parameters at 3 V (Table 1) indicate a still large but reduced time constant, showing that the dominant relaxation process is shifting toward faster charge transport in the $MoSe_2$/SWNT network. Moreover, the plot shows an increased scatter in the lowest-frequency points below ~160 Hz, which we attribute to long-time drift and the onset of slower auxiliary processes not resolved as a separate semicircle in the measured frequency window. The $MoSe_2$/SWNT interface plays a crucial role, as the highly conductive SWNT core acts as an electron reservoir, modulating charge transport through the surrounding $MoSe_2$ shell. The formation of conductive percolation pathways within the $MoSe_2$ domains is likely driven by field-induced carrier delocalization within the defect-rich $MoSe_2$ regions and charge hopping between localized trap sites.[3,92]

At higher voltages (4 V–5 V), the semicircle becomes more pronounced and complete, and the resistance drops to 3.52 MΩ at 4 V and 2.37 MΩ at 5 V (Table 1). The Nyquist plots at these voltages are well described by a single depressed semicircle that rises essentially from the origin, indicating that no distinct high-frequency charge-transfer resistance can be resolved and that the impedance is dominated by bulk processes in the $MoSe_2$/SWNT network.[66] The lowest-frequency points (<~200 Hz) exhibit some fluctuation, which we ascribe to measurement drift rather than a well-developed Warburg-type diffusion tail. The decrease in CPE values at these voltages suggests that charge storage mechanisms are less significant, and the device exhibits predominantly resistive behaviour. The characteristic time constant extracted from the 5 V spectrum is $\tau \approx 1.2$ ms, which we treat as the dominant time scale of the device in the subsequent reservoir-computing analysis. The system behaves more like an ideal resistor with minimal capacitive effects at this stage.

The *I–V* measurements further support this resistive switching behaviour. At low voltages, the device exhibits a near-Ohmic response, likely dominated by trap-limited conduction. However, under AC excitation (as in EIS), the same voltage range shows a capacitive-dominated response with high impedance, suggesting significant charge trapping and limited carrier mobility. As the voltage increases, the device transitions into the trap-filled limit (TFL) region, characteristic of the

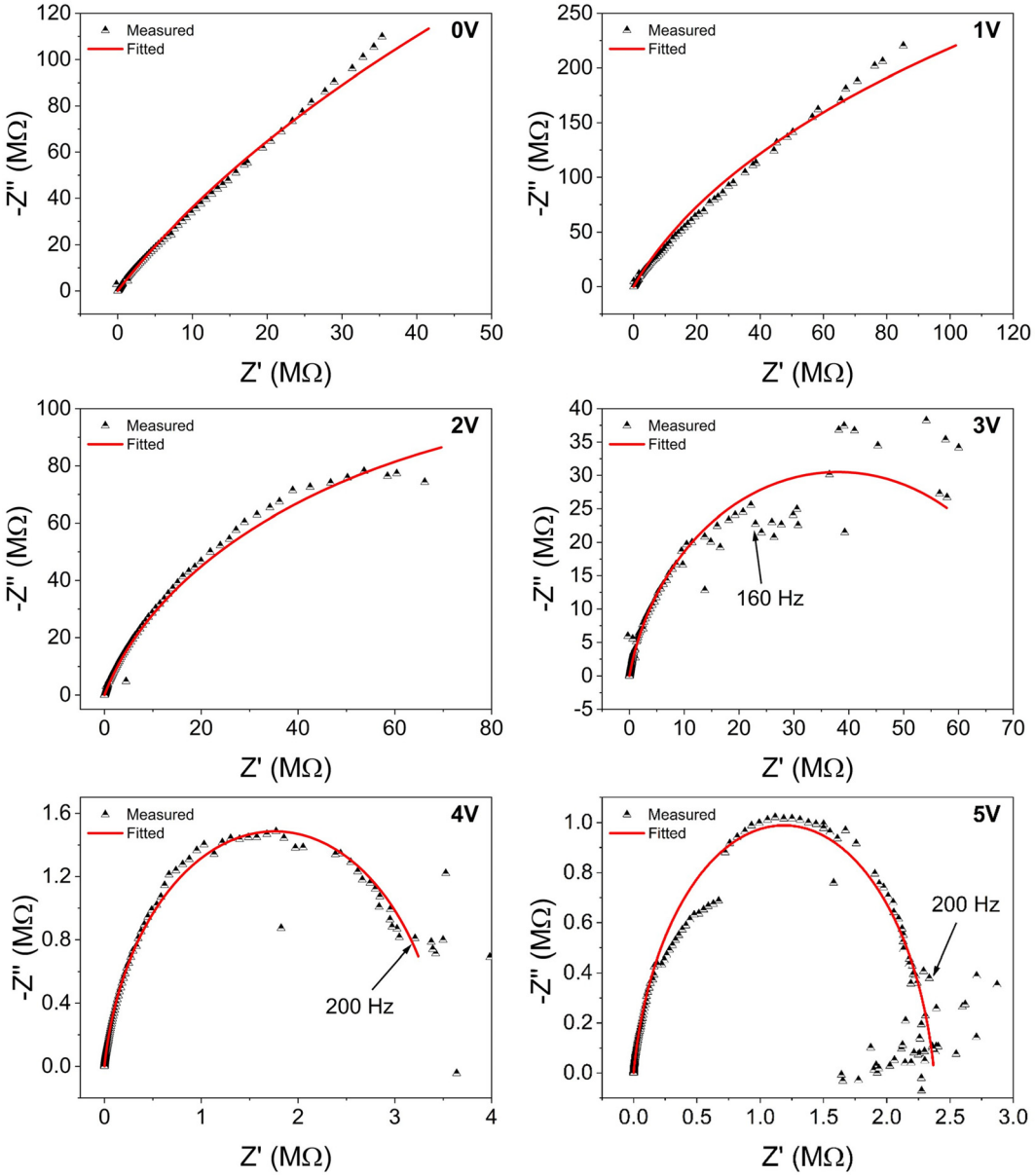

Fig. 4 EIS measurements for different DC offset voltages where the perturbation AC voltage was set to 300 mV. All measurements were performed in the 1 Hz–1 MHz range. The inset arrows show the frequencies where the fluctuations start to stabilize.

Table 1 Values obtained after fitting to the *R*/CPE equivalent circuit

Voltage	R (MΩ)	Q (nΩ^{-1} s^{n})	n	τ (s)
0 V	1000.00	1.67	0.851	≈1.83 s
1 V	1000.00	0.76	0.878	≈0.73 s
2 V	246.00	1.49	0.858	≈0.31 s
3 V	76.10	1.33	0.860	≈0.07 s
4 V	3.52	1.04	0.893	≈1.90 ms
5 V	2.37	1.13	0.885	≈1.20 ms

SCLC mechanism[47,88,93] where the filling of traps can produce a sharp increase in current once the trap-filled limit is reached. This provides a natural explanation for the abrupt SET transition without the need to assume metallic filament formation. Both the HRS and LRS *I–V* curves can be fitted with SCLC-type power laws over a broad voltage range, indicating that space-charge-limited transport in the $MoSe_2$/SWNT bulk is the dominant conduction mechanism, while any interfacial or redox contributions are not resolved as separate elements in the EIS spectra. The coexistence of Ohmic-like behaviour in the DC *I–V* and capacitive response in EIS highlights the complex interplay of resistive and dielectric effects in the high-resistance state. This duality is further confirmed as the system transitions to a low resistance, predominantly the resistive state at higher voltages.

3.4. PRC tasks

3.4.1. Waveform reconstruction benchmark tasks. The goal is to employ the $MoSe_2$/SWNT core–shell structure as a reservoir in a reservoir computing framework to transform input signals into a high-dimensional space, facilitating complex signal processing tasks. By feeding a sine wave with a fundamental frequency of 11 Hz into the device, we observed its output through FFT analysis, as shown in Fig. S2 in the SI, revealing the presence of harmonics at integer multiples of the input frequency (22 Hz, 33 Hz, *etc.*). This harmonic generation indicates nonlinearity in the device's response, a desirable characteristic for effective reservoir computing.

To evaluate the device's capability for nonlinear transformation and periodic signal modelling, ridge regression was applied to fit its 15 output signals to various target waveforms, as illustrated in Fig. 5. These included cosine, triangle, sawtooth, square, and sinusoidal waves at higher harmonic frequencies. The results showed consistently low NMSE values (all below 0.1), with accuracy metrics presented in Table 2. The cosine waveform (Fig. 5a), comprising a single frequency component, was reconstructed with 99.9% accuracy, demonstrating that the device can reliably preserve both the amplitude and phase of fundamental harmonic content. Triangle (Fig. 5b) and square waves (Fig. 5c), which consist of odd harmonics, were also reconstructed with high accuracy (99.7% and 93.5%, respectively), indicating that the device effectively captures both smooth and abrupt waveform features. For the sawtooth waveform (Fig. 5d), which contains both odd and even harmonics with linearly decreasing amplitude, the reservoir successfully reproduced its asymmetric profile, achieving 89.0% accuracy.

Performance on higher-order sinusoidal waveforms further confirmed the device's nonlinear capacity. The Sin2ω waveform (Fig. 5e) was fitted with 99.7% accuracy, while the more complex Sin3ω waveform (Fig. 5f) achieved 95.1%. These results suggest that the reservoir retains sufficient nonlinearity

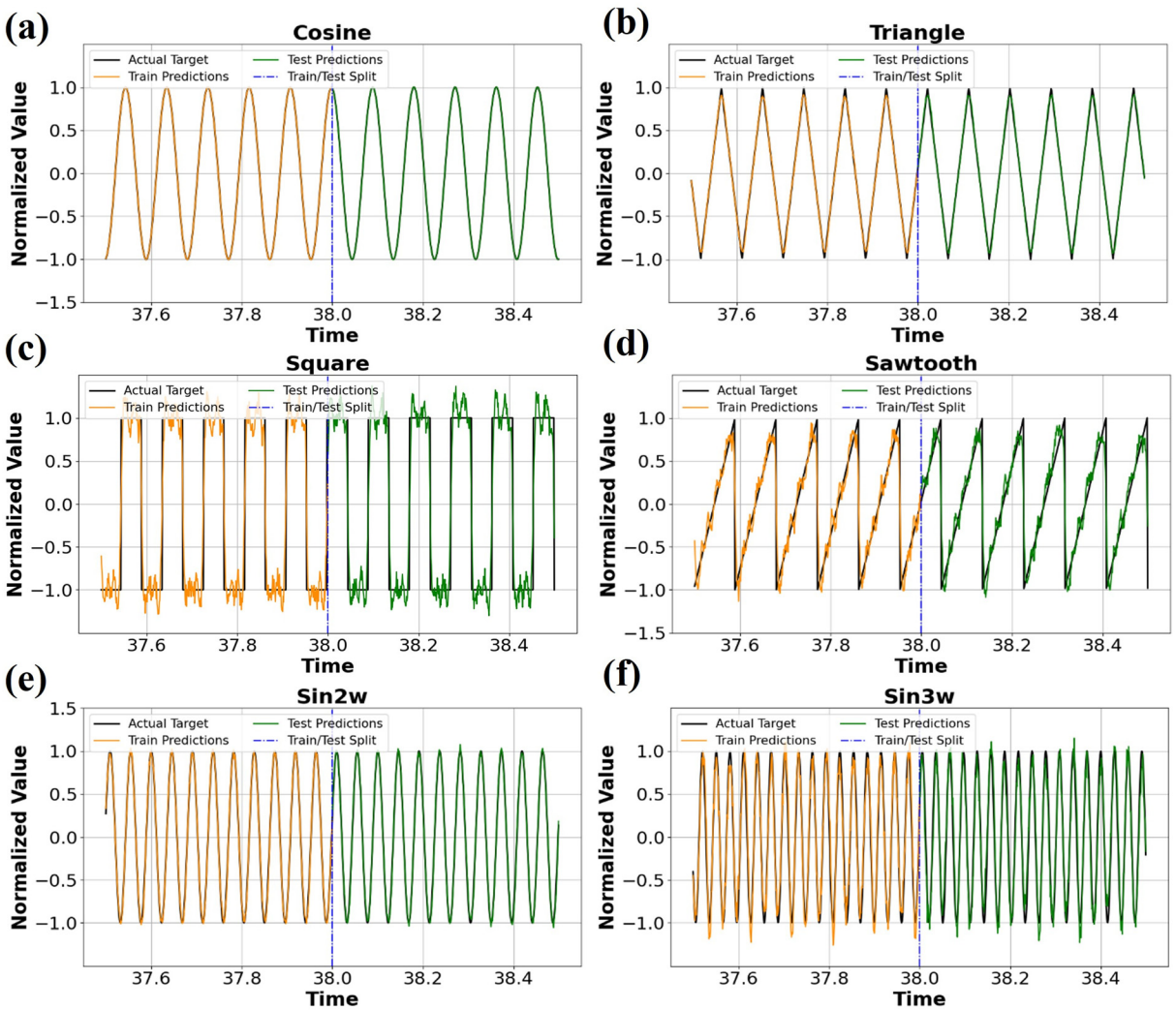

Fig. 5 Waveform reconstruction task representation with the target wave (black line), the training wave (orange), and the predicted wave (green), respectively. Accuracies for: (a) cosine: 99.9%, (b) triangle: 99.7%, (c) square: 93.5%, (d) sawtooth: 89.0%, (e) Sin2ω: 99.7%, and (f) Sin3ω: 95.1%.

Table 2 Waveform reconstruction accuracy comparison of different in-materio reservoir computing systems. The table highlights both task accuracy and the underlying conduction mechanism, showing how device physics correlates with computational performance

		Waveform fitting accuracy (%)				
Device structure/materials	Conduction mechanism	Cosine	Triangle	Sawtooth	Square	Sin2ω
Ag_2S polycrystalline film[39]	Filamentary	98.6	94.3	75.4	89.7	
SWNT/Por-POM complexes[40]	Redox	99.0	99.4	71.0	87.0	
SPAN electrochemical network[20]	Redox	99.0		88.0	91.0	93.0
Ag_2Se nanowire[8]	Filamentary	99.8	98.6	62.3	82.1	
SWNT/H_4TPP-POM complexes[94]	Redox		99.0	72.0	86.0	79.0
Ag nanowire[95]	Filamentary	97.0		86.0	83.0	87.0
Ag–Ag_2S nanoparticle[35]	Filamentary	99.9	98.3	70.2	87.5	
RR-P3HT thin film[42]	Molecular orientation	99.0	99.0	65.0	85.0	61.0
$MoSe_2$/SWNT core–shell (this work)	**SCLC**	**99.9**	**99.7**	**89.0**	**93.5**	**99.7**

to support the reconstruction of signals composed of higher harmonic content. Together, these findings highlight the $MoSe_2$/SWNT device's effectiveness as a physical reservoir for waveform reconstruction, capable of handling a wide range of periodic structures from fundamental components to more complex, harmonically rich signals. We compared our results up to Sin2ω on this task with those of other works and summarized them in Table 2.

The comparison in Table 2 underscores the strong influence of the conduction mechanism on task performance. Filamentary systems such as Ag_2S, Ag nanowires, and Ag–Ag_2S exhibit nonlinear dynamics that enable waveform fitting but often result in reduced accuracy for harmonically rich signals such as sawtooth and square waves. Ionic or redox-based polymer systems (SPAN and SWNT-POM) provide improved performance on some temporal tasks but remain limited in harmonic preservation. In contrast, the $MoSe_2$/SWNT device operating in the SCLC regime achieves consistently high accuracy across all waveforms, particularly for higher-order harmonics (Sin2ω = 99.7%). This advantage arises from higher harmonic generation and short-term memory in the trap-controlled conduction process. FFT analysis of the device outputs (Fig. S2) clearly shows pronounced peaks at the fundamental and harmonic frequencies, while Lissajous plots (Fig. S3) reveal asymmetric ellipses and hysteresis, both confirming rich nonlinear dynamics that support accurate waveform reconstruction. Fig. S4 shows the Total Harmonic Distortion (THD) measurements, revealing a heterogeneous distribution of nonlinearity across the electrodes that is essential for rich feature encoding. The raw experimental signals are presented in Fig. S5, where the output waveform exhibits clear distortion compared to the sinusoidal input, confirming the nonlinear transformation capabilities of the device. These results highlight how SCLC dynamics provide a more favourable basis for nonlinear transformation compared to filamentary or redox systems. Furthermore, the input and output waveforms for the NARMA and memory capacity (MC) tasks, utilizing uniform white noise as the input signal, are illustrated in Fig. S6.

3.4.2. NARMA2 prediction tasks. The NARMA2 task, a widely used benchmark for assessing the computational capacity of reservoir systems, was employed to evaluate the performance of the $MoSe_2$/SWNT core–shell device. This task tests the device's ability to handle nonlinear dynamics and short-term memory, both crucial for reservoir computing applications. The goal of the NARMA2 task is to predict the future values of a nonlinear autoregressive moving average process of order 2, based on the past inputs.[74–76] The results are shown in Fig. 6. In the upper plot, the blue points represent the model's predictions during training, while the orange points represent the predictions during testing. The grey line shows the target NARMA2 values, providing a reference for comparison. The model was trained on 800 time steps, and the transition between the training and test phases is marked by a vertical green line. During the test phase, the model was tasked with predicting the next 200 time steps based solely on the past inputs without further training.

During the training phase, the predictions closely follow the target values, demonstrating that the device successfully learned the underlying dynamics of the NARMA2 task. The alignment between the blue points (predictions) and the grey line (target) indicates that the device effectively modelled the nonlinear relationships inherent in the NARMA2 system. In the testing phase, represented by the orange points, the device continued to perform well, closely tracking the target values with only minor deviations. The bottom plot zooms in on the 200 test points to provide a clearer view of the model's predictive performance. The red points indicate the predicted values, while the grey line corresponds to the actual target values. The device's ability to follow the oscillations and fluctuations of the NARMA2 time series is evident, as most predicted points align closely with the target. Although there are occasional small deviations, the overall performance remains robust. The model achieved an accuracy of 90% on the NARMA2 task, indicating the device's strong capability in handling complex, nonlinear temporal dependencies. The remaining 10% error can be attributed to small discrepancies between the predicted and target values, especially during periods of rapid fluctuation in the NARMA2 time series. Nonetheless, the high accuracy suggests that the $MoSe_2$/SWNT core–shell device can effectively process and model complex time-series data.

3.4.3. Memory capacity. The memory capacity (MC) task is another important benchmark for evaluating the compu-

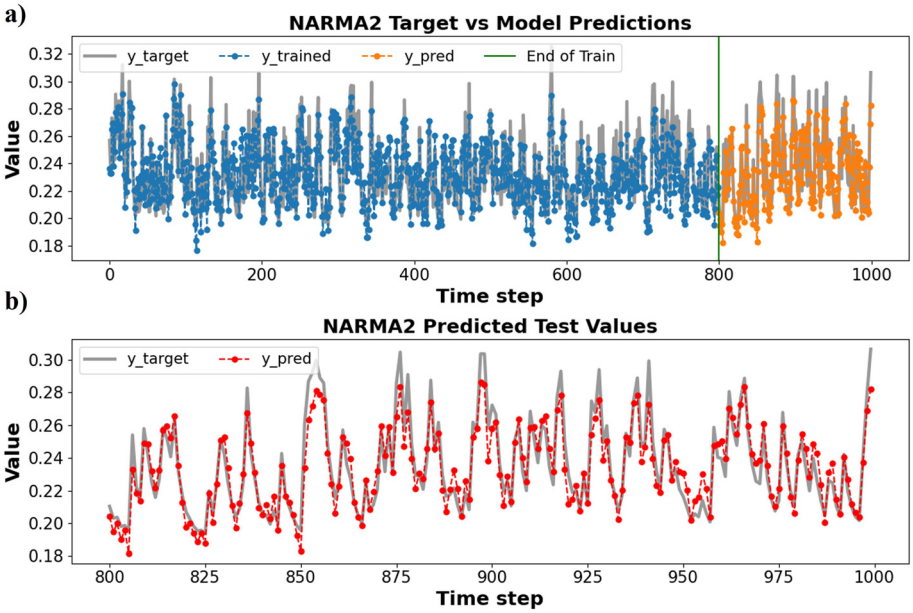

Fig. 6 NARMA2 prediction task. (a) The full plot showing both training and the predicted plot with a total of 1000 data points used. (b) The zoomed plot of the 200 datapoints of the prediction of 90% accuracy.

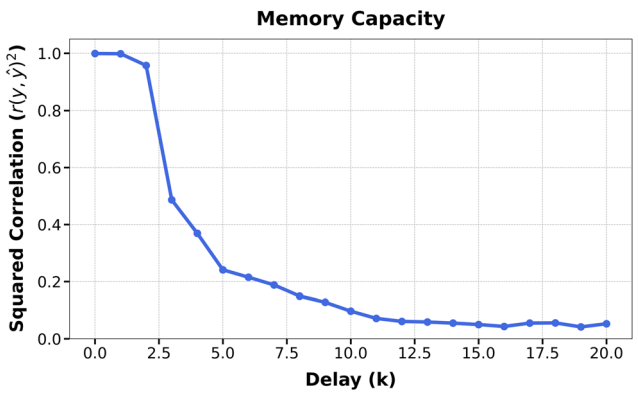

Fig. 7 Memory capacity of the $MoSe_2$/SWNT device with the noise input.

tational abilities of a reservoir system, specifically its ability to retain information over time. In this task, the device is evaluated on its ability to recall previous inputs after a specified delay. Memory capacity is crucial in tasks like time-series prediction, where the system needs to retain past information to make accurate future predictions. This task directly complements the NARMA2 task, as both rely on the device's ability to process and retain temporal information effectively.[9,74,96]

Fig. 7 shows the squared correlation (Cor^2) between the input signal and the reservoir's output as a function of the delay. The memory capacity (MC) is determined by summing the squared correlation values across different delays, with a higher MC indicating that the reservoir can recall information from further back in time. For this device, the total memory capacity was found to be 5.2, meaning that the system can effectively retain and utilize information over approximately 5 time steps.

Examining the plot, the squared correlation reaches a maximum value of 1.0 at zero delay, indicating that the system perfectly retains the current input. As the delay increases, the correlation drops steeply, showing that the device's ability to recall past inputs decreases rapidly. By the time the delay reaches around 5 steps, the correlation drops to approximately 0.2, indicating that the system still retains some memory, but it has significantly decayed. Beyond 10 delays, the correlation becomes quite small, reflecting that the system has little memory of inputs from that far in the past. This result is consistent with the device's performance on the NARMA2 task. A memory capacity of 5.2 indicates that the device can handle tasks requiring short-term memory over a few time steps. In the NARMA2 task, where the system needs to predict the next value based on the past two inputs, this level of memory capacity is sufficient to capture the required temporal dependencies, which explains the relatively high accuracy of 90% achieved in the NARMA2 task. The NARMA2 task, with its short-term memory requirement, aligns well with the observed memory capacity of the device, as it requires the system to retain relevant information for a small number of time steps.

4. Conclusion

In conclusion, the $MoSe_2$/SWNT core–shell structure demonstrates significant promise as a physical reservoir for neuromorphic computing applications. The unique combination of the high conductivity provided by SWNTs and the semiconducting, nonlinear characteristics of $MoSe_2$ enables the device

to exhibit pronounced memristive switching and dynamic behaviour under different electrical biases. Detailed experimental analyses confirmed that the device transitions from a capacitive-dominated high-resistance state to a resistive low-resistance state with clear SCLC behaviour, essential for effective reservoir computing. Performance in benchmark tasks such as waveform reconstruction, NARMA2 prediction, and memory capacity tests validates the ability of the material system to transform input signals into high-dimensional representations, making it a strong candidate for future AI hardware. While this study established the fundamental SCLC dynamics and baseline performance on NARMA2, future investigations will extend this platform to higher-order temporal tasks, such as speech recognition and handwritten digit recognition, to further validate the system's scalability for real-world neuromorphic applications. By offering a designless, bottom-up approach for neuromorphic computing, this work opens new pathways toward ultra-low-power, flexible, and scalable artificial intelligence hardware that could enable next-generation applications in robotics, edge computing, and beyond.

Author contributions

A. S. K. Z.: conceptualization, data curation, methodology, software, validation, visualization, investigation, and writing – original draft. S. A.: investigation, software, and review & editing. M. X.: funding acquisition and review & editing. Y. U.: funding acquisition and review & editing. H. T.: resources, conceptualization, validation, project administration, supervision, and review & editing of the manuscript draft.

Conflicts of interest

The authors declare that they have no conflicts of interest.

Data availability

The authors confirm that the data supporting the findings of this study are available within the article and its supplementary information (SI). Supplementary information is available. See DOI: https://doi.org/10.1039/d5nr03974f.

Raw data that support the findings of this study are available from the corresponding author upon reasonable request.

Acknowledgements

This work was supported by Japan Society for the Promotion of Science (JSPS), KAKENHI (grant no. 22H01900, 23K17864, 23K18495, 25K17938, and 25K21341), Japan Science and Technology Agency (JST) CREST (grant no. JPMJCR21B5), JST ACT-X (grant no. JPMJAX22K4), JST ALCA-Next (grant no. JPMJAN23F3), and the JSPS Core-to-Core Program (JPJSCCA20220006).

References

1 D. Przyczyna, P. Zawal, T. Mazur, M. Strzelecki, P. L. Gentili and K. Szaciłowski, *Jpn. J. Appl. Phys.*, 2020, **59**, 050504.
2 R. Fang, W. Zhang, K. Ren, P. Zhang, X. Xu, Z. Wang and D. Shang, *Mater. Futures*, 2023, **2**, 022701.
3 V. K. Sangwan and M. C. Hersam, *Nat. Nanotechnol.*, 2020, **15**, 517–528.
4 F. Hadaeghi, *Natural Computing Series*, 2021, pp. 221–237.
5 G. Tanaka, T. Yamane, J. B. Héroux, R. Nakane, N. Kanazawa, S. Takeda, H. Numata, D. Nakano and A. Hirose, *Neural Networks*, 2019, **115**, 100–123.
6 G. Abdi, T. Mazur and K. Szaciłowski, *Jpn. J. Appl. Phys.*, 2024, **63**, 050803.
7 R. Islam, H. Li, P.-Y. Chen, W. Wan, H.-Y. Chen, B. Gao, H. Wu, S. Yu, K. Saraswat and H.-S. Philip Wong, *J. Phys. D: Appl. Phys.*, 2019, **52**, 113001.
8 T. Kotooka, S. Lilak, A. Z. Stieg, J. K. Gimzewski, N. Sugiyama, Y. Tanaka, T. Kawabata, A. Karacali, H. Tamukoh, Y. Usami and H. Tanaka, *Adv. Electron. Mater.*, 2024, 2400443.
9 I. T. Vidamour, C. Swindells, G. Venkat, L. Manneschi, P. W. Fry, A. Welbourne, R. M. Rowan-Robinson, D. Backes, F. Maccherozzi, S. S. Dhesi, E. Vasilaki, D. A. Allwood and T. J. Hayward, *Commun. Phys.*, 2023, **6**, 1–11.
10 H. Zhang and D. V. Vargas, *IEEE Access*, 2023, **11**, 81033–81070.
11 A. Jalalvand, K. Demuynck, W. De Neve and J. P. Martens, *Neurocomputing*, 2018, **277**, 237–248.
12 M. Lukoševičius and H. Jaeger, *Comput. Sci. Rev.*, 2009, **3**, 127–149.
13 W. Jiang, L. Chen, K. Zhou, L. Li, Q. Fu, Y. Du and R. H. Liu, *Appl. Phys. Lett.*, 2019, **115**, 192403.
14 Y. Yamazaki and K. Kinoshita, *Adv. Sci.*, 2024, **11**, 1–9.
15 M. Hakoshima, Y. Usami, T. Kotooka and H. Tanaka, *Jpn. J. Appl. Phys.*, 2023, **62**, SG1042.
16 R. Zhu, S. Lilak, A. Loeffler, J. Lizier, A. Stieg, J. Gimzewski and Z. Kuncic, *Nat. Commun.*, 2023, **14**, 1–16.
17 M. Farronato, P. Mannocci, M. Melegari, S. Ricci, C. M. Compagnoni and D. Ielmini, *Adv. Mater.*, 2022, 2205381.
18 Y. Zhong, J. Tang, X. Li, B. Gao, H. Qian and H. Wu, *Nat. Commun.*, 2021, **12**, 1–9.
19 G. Milano, M. Luebben, Z. Ma, R. Dunin-Borkowski, L. Boarino, C. F. Pirri, R. Waser, C. Ricciardi and I. Valov, *Nat. Commun.*, 2018, **9**, 5151.
20 Y. Usami, B. Ven, D. G. Mathew, T. Chen, T. Kotooka, Y. Kawashima, Y. Tanaka, Y. Otsuka, H. Ohoyama, H. Tamukoh, H. Tanaka, W. G. Wiel and T. Matsumoto, *Adv. Mater.*, 2021, **33**, 2102688.
21 G. Milano, K. Montano and C. Ricciardi, *J. Phys. D: Appl. Phys.*, 2023, **56**, 084005.
22 G. Milano, G. Pedretti, K. Montano, S. Ricci, S. Hashemkhani, L. Boarino, D. Ielmini and C. Ricciardi, *Nat. Mater.*, 2022, **21**, 195–202.

23 E. C. Demis, R. Aguilera, K. Scharnhorst, M. Aono, A. Z. Stieg and J. K. Gimzewski, *Jpn. J. Appl. Phys.*, 2016, **55**, 1102B2.
24 Z. Kuncic and T. Nakayama, *Adv. Phys.: X*, 2021, **6**, 1894234.
25 A. Loeffler, A. Diaz-Alvarez, R. Zhu, N. Ganesh, J. M. Shine, T. Nakayama and Z. Kuncic, *Sci. Adv.*, 2023, **9**, 1–15.
26 S. Lilak, W. Woods, K. Scharnhorst, C. Dunham, C. Teuscher, A. Z. Stieg and J. K. Gimzewski, *Front. Nanotechnol.*, 2021, **3**, 1–11.
27 K. S. Scharnhorst, J. P. Carbajal, R. C. Aguilera, E. J. Sandouk, M. Aono, A. Z. Stieg and J. K. Gimzewski, *Jpn. J. Appl. Phys.*, 2018, **57**, 1–6.
28 R. Zhu, S. Lilak, A. Loeffler, J. Lizier, A. Stieg, J. Gimzewski and Z. Kuncic, *Nat. Commun.*, 2023, **14**, 6697.
29 K. Montano, G. Milano and C. Ricciardi, *Neuromorphic Comput. Eng.*, 2022, **2**, 014007.
30 G. Milano, G. Pedretti, K. Montano, S. Ricci, S. Hashemkhani, L. Boarino, D. Ielmini and C. Ricciardi, *Nat. Mater.*, 2022, **21**, 195–202.
31 G. Milano, M. Luebben, Z. Ma, R. Dunin-Borkowski, L. Boarino, C. F. Pirri, R. Waser, C. Ricciardi and I. Valov, *Nat. Commun.*, 2018, **9**, 1–10.
32 T. T. Dang, O. Srikimkaew, D. Banerjee, S. Azhari, Y. Usami and H. Tanaka, *Appl. Phys. Lett.*, 2024, **124**, 091903.
33 O. Srikimkaew, S. Ricci, M. Porzani, T. T. Dang, Y. Nakaoka, Y. Usami, D. Ielmini and H. Tanaka, *Adv. Electron. Mater.*, 2024, **10**, 2300709.
34 O. Srikimkaew, S. Azhari, D. Banerjee, Y. Usami and H. Tanaka, *Adv. Electron. Mater.*, 2024, **10**, 2400360.
35 O. Srikimkaew, D. Banerjee, S. Azhari, Y. Usami and H. Tanaka, *ACS Appl. Electron. Mater.*, 2024, **6**, 688–695.
36 R. Matsuo and T. Hasegawa, *Jpn. J. Appl. Phys.*, 2024, **63**, 03SP61.
37 K. Yoshimura and T. Hasegawa, *Jpn. J. Appl. Phys.*, 2024, **63**, 03SP17.
38 A. Mizuno, Y. Ohno, M. Hayakawa, K. Yoshimura and T. Hasegawa, *Jpn. J. Appl. Phys.*, 2024, **63**, 02SP60.
39 K. Yoshimura, H. Tanaka and T. Hasegawa, *Jpn. J. Appl. Phys., Part 1*, 2025, **64**, 03SP05.
40 D. Banerjee, T. Kotooka, S. Azhari, Y. Usami, T. Ogawa, J. K. Gimzewski, H. Tamukoh and H. Tanaka, *Adv. Intell. Syst.*, 2022, **4**, 2100145.
41 G. Abdi, A. Karacali, A. S. K. Zaman, M. Gryl, A. Sławek, A. Szkudlarek, H. Tanaka and K. Szaciłowski, *Adv. Electron. Mater.*, 2025, **11**, e00049.
42 M. Desu, A. Karacali, Y. Usami, Y. Ishizaki-Betchaku, S. Nagano, M. Xu, S. S. Pandey and H. Tanaka, *Jpn. J. Appl. Phys., Part 1*, 2025, **64**, 04SP12.
43 B. He, G. Li, J. Li, J. Wang, H. Tong, Y. Fan, W. Wang, S. Sun and F. Dang, *Adv. Energy Mater.*, 2021, **11**, 2003263.
44 R. Dutt, R. R. Srivastava, H. Mishra and A. Srivastava, *Opt. Mater.*, 2024, **149**, 115050.
45 L. Lee, C. H. Chiang, Y. C. Shen, S. C. Wu, Y. C. Shih, T. Y. Yang, Y. C. Hsu, R. H. Cyu, Y. J. Yu, S. H. Hsieh, C. H. Chen, M. Lebedev and Y. L. Chueh, *ACS Nano*, 2023, **17**, 84–93.
46 K. Sk, B. Das, N. Chakraborty, M. Samanta, S. Bera, A. Bera, D. S. Roy, S. K. Pradhan, K. K. Chattopadhyay and M. Mondal, *Adv. Opt. Mater.*, 2022, **10**, 2200791.
47 B. Das, A. Bera, M. Samanta, S. Bera, S. Kalimuddin, M. Kundu, S. Gayen, K. K. Chattopadhyay and M. Mondal, *ACS Appl. Electron. Mater.*, 2021, **3**, 3096–3105.
48 M. Mirzaei and M. B. Gholivand, *J. Taiwan Inst. Chem. Eng.*, 2022, **135**, 104378.
49 A. Singh, D. Poddar, S. Thakur and R. Jha, *Mater. Chem. Phys.*, 2021, **273**, 125043.
50 M. Kladkaew, J. Y. Lin, N. Chanlek, V. Vailikhit and P. Hasin, *ACS Appl. Energy Mater.*, 2023, **6**, 397–415.
51 W. Xue, W. Ci, X.-H. Xu and G. Liu, *Chin. Phys. B*, 2020, **29**, 048401.
52 M. E. Pereira, R. Martins, E. Fortunato, P. Barquinha and A. Kiazadeh, *Neuromorphic Comput. Eng.*, 2023, **3**, 022002.
53 T. Hotta, H. Nakajima, S. Chiashi, T. Inoue, S. Maruyama, K. Watanabe, T. Taniguchi and R. Kitaura, *Appl. Phys. Express*, 2022, **16**, 015001.
54 L. Hu, Y. C. Huang, Y. J. Huang, P. H. Lin, H. C. Wang, C. K. Lin and K. Y. Lee, *Nanotechnology*, 2024, **35**, 465502.
55 Y. Huang, H. Lu, H. Gu, J. Fu, S. Mo, C. Wei, Y. E. Miao and T. Liu, *Nanoscale*, 2015, **7**, 18595–18602.
56 S.-Y. Bae, I.-Y. Jeon, J. Mahmood and J.-B. Baek, *Chem. Eur. J.*, 2018, **24**, 18158–18179.
57 I. S. Kwon, I. H. Kwak, T. T. Debela, H. G. Abbas, Y. C. Park, J. P. Ahn, J. Park and H. S. Kang, *ACS Nano*, 2020, **14**, 6295–6304.
58 J. Yang, Y. Liu, C. Shi, J. Zhu, X. Yang, S. Liu, L. Li, Z. Xu, C. Zhang and T. Liu, *ACS Appl. Energy Mater.*, 2018, **1**, 7035–7045.
59 Z. Lei, S. Xu and P. Wu, *Phys. Chem. Chem. Phys.*, 2016, **18**, 70–74.
60 U. Gupta, B. S. Naidu, U. Maitra, A. Singh, S. N. Shirodkar, U. V. Waghmare and C. N. R. Rao, *APL Mater.*, 2014, **2**, 092802.
61 S. S. Karade, A. S. Nimbalkar, J. H. Eum and H. Kim, *RSC Adv.*, 2020, **10**, 40092–40105.
62 Y. Liu, W. Li, X. Chang, H. Chen, X. Zheng, J. Bai and Z. Ren, *J. Colloid Interface Sci.*, 2020, **562**, 483–492.
63 Y. P. Gao, X. Wu, K. J. Huang, L. L. Xing, Y. Y. Zhang and L. Liu, *CrystEngComm*, 2017, **19**, 404–418.
64 J. Yin, H. Chen, W. Lu, M. Liu, I. Ling Li, M. Zhang, W. Zhang, J. Wang, Z. Xu, P. Yan, W. Liu and S. Ruan, *Nanotechnology*, 2017, **28**, 484001.
65 C. Zhang, J. Zhang, Y. Fu, J. Liu, S. Wang and Y. Wang, *Ionics*, 2023, **29**, 941–950.
66 A. Sławek, L. Alluhaibi, E. Kowalewska, G. Abdi, T. Mazur, A. Podborska, K. Mech, M. Marciszko-Wiąckowska, A. Maximenko and K. Szaciłowski, *Adv. Electron. Mater.*, 2024, **10**, 2300818.
67 D. Banerjee, S. Azhari, Y. Usami and H. Tanaka, *Appl. Phys. Express*, 2021, **14**, 105003.
68 Y. Yan, B. Sun and D. Ma, *Chem. Phys. Lett.*, 2015, **638**, 103–107.

69 Y. Wang, J. Yang, Z. Wang, J. Chen, Q. Yang, Z. Lv, Y. Zhou, Y. Zhai, Z. Li and S. T. Han, *Small*, 2019, **15**, 1805431.
70 R. Marquardt, F. Zahari, J. Carstensen, G. Popkirov, O. Gronenberg, G. Kolhatkar, H. Kohlstedt and M. Ziegler, *Adv. Electron. Mater.*, 2023, **9**, 2201227.
71 S. Maity, B. Das, M. Samanta, B. K. Das, S. Ghosh and K. K. Chattopadhyay, *ACS Appl. Energy Mater.*, 2020, **3**, 5067–5076.
72 N. Dragoe and N. Dragoe, *Mater. Lab*, 2024, **3**, 230031–230031.
73 A. C. Lazanas and M. I. Prodromidis, *ACS Meas. Sci. Au*, 2023, **3**, 162–193.
74 S. Kan, K. Nakajima, T. Asai and M. Akai-Kasaya, *Adv. Sci.*, 2022, **9**, 1–8.
75 D. Nishioka, T. Tsuchiya, W. Namiki, M. Takayanagi, M. Imura, Y. Koide, T. Higuchi and K. Terabe, *Sci. Adv.*, 2022, **8**, 1–14.
76 S. Kan, K. Nakajima, Y. Takeshima, T. Asai, Y. Kuwahara and M. Akai-Kasaya, *Phys. Rev. Appl.*, 2021, **15**, 024030.
77 M. Yousaf, Y. Wang, Y. Chen, Z. Wang, W. Aftab, A. Mahmood, W. Wang, S. Guo and R. P. S. Han, *ACS Appl. Mater. Interfaces*, 2018, **10**, 14622–14631.
78 M. Yousaf, Y. Wang, Y. Chen, Z. Wang, A. Firdous, Z. Ali, N. Mahmood, R. Zou, S. Guo and R. P. S. Han, *Adv. Energy Mater.*, 2019, **9**, 1900567.
79 H. Mittal and M. Khanuja, *Environ. Sci. Pollut. Res.*, 2020, **27**, 23477–23489.
80 S. Vishwanath, X. Liu, S. Rouvimov, P. C. Mende, A. Azcatl, S. McDonnell, R. M. Wallace, R. M. Feenstra, J. K. Furdyna, D. Jena and H. G. Xing, *2D Mater.*, 2015, **2**, 024007.
81 Y. Xia, W. Zhu, Q. Zhu, J. Wu, Z. Nie, W. Zhang, S. Zheng and S. Qi, *J. Mater. Sci.: Mater. Electron.*, 2021, **32**, 25795–25808.
82 V. K. Ksenevich, N. I. Gorbachuk, H. Viet, M. V. Shuba, A. G. Paddubskaya and A. D. Wieck, *Nonlinear Phenom. Complex Syst.*, 2017, **20**, 360–367.
83 R. Kaur, K. P. Singh and S. K. Tripathi, *J. Alloys Compd.*, 2022, **905**, 164103.
84 J. Kistner-Morris, A. Shi, E. Liu, T. Arp, F. Farahmand, T. Taniguchi, K. Watanabe, V. Aji, C. H. Lui and N. Gabor, *Nat. Commun.*, 2024, **15**, 1–7.
85 Z. Zhang, D. Yang, H. Li, C. Li, Z. Wang, L. Sun and H. Yang, *Neuromorphic Comput. Eng.*, 2022, **2**, 032004.
86 L. Hu, D. S. Hecht and G. Gruner, *Nano Lett.*, 2004, **4**, 2513–2517.
87 P. S. Kang and G. T. Kim, *Phys. Status Solidi B*, 2011, **248**, 2644–2648.
88 B. R. Naik, N. Arya and V. Balakrishnan, *Nanotechnology*, 2024, **35**, 215201.
89 G. Zhou, B. Sun, Y. Yao, H. Zhang, A. Zhou, K. Alameh, B. Ding and Q. Song, *Appl. Phys. Lett.*, 2016, **109**, 143904.
90 M. Xu, K. Furuta, A. Karacali, Y. Umezaki, A. S. Kamarol Zaman, Y. Usami, H. Tanaka and Y. Horibe, *Small*, 2025, **21**, e06397.
91 K. A. Nirmal, D. D. Kumbhar, A. V. Kesavan, T. D. Dongale and T. G. Kim, *npj 2D Mater. Appl.*, 2024, **8**, 1–27.
92 E. W. Lim and R. Ismail, *Electronics*, 2015, **4**, 586–613.
93 X. Xia, W. Huang, P. Hang, T. Guo, Y. Yan, J. Yang, D. Yang, X. Yu and X. Li, *ACS Mater. Lett.*, 2023, **5**, 1109–1135.
94 Y. Usami, S. Murazoe, D. Banerjee, T. Kotooka and H. Tanaka, *Appl. Phys. Lett.*, 2025, **126**, 83504.
95 F. Michieletti, D. Pilati, G. Milano and C. Ricciardi, *Adv. Funct. Mater.*, 2025, **35**, 2423903.
96 T. Schulte to Brinke, M. Dick, R. Duarte and A. Morrison, *Sci. Rep.*, 2023, **13**, 1–16.